Kinetic and Structural Impact of Metal Ions and Genetic Variations on Human DNA Polymerase ι*[S]

Jeong-Yun Choi[‡], Amritaj Patra[§], Mina Yeom[‡], Young-Sam Lee[¶], Qianqian Zhang[§], Martin Egli[§], and F. Peter Guengerich[§1]

From the [‡]Division of Pharmacology, Department of Molecular Cell Biology, Samsung Biomedical Research Institute, Sungkyunkwan University School of Medicine, Gyeonggi-do 16419, Republic of Korea, the [§]Department of Biochemistry, Vanderbilt University School of Medicine, Nashville, Tennessee 37232-0146, and the [¶]Department of New Biology, Daegu Gyeongbuk Institute of Science and Technology, Daegu 42988, Republic of Korea

DNA polymerase (pol) ι is a Y-family polymerase involved in translesion synthesis, exhibiting higher catalytic activity with Mn^{2+} than Mg^{2+}. The human germline R96G variant impairs both Mn^{2+}-dependent and Mg^{2+}-dependent activities of pol ι, whereas the Δ1–25 variant selectively enhances its Mg^{2+}-dependent activity. We analyzed pre-steady-state kinetic and structural effects of these two metal ions and genetic variations on pol ι using pol ι core (residues 1–445) proteins. The presence of Mn^{2+} (0.15 mM) instead of Mg^{2+} (2 mM) caused a 770-fold increase in efficiency ($k_{pol}/K_{d,dCTP}$) of pol ι for dCTP insertion opposite G, mainly due to a 450-fold decrease in $K_{d,dCTP}$. The R96G and Δ1–25 variants displayed a 53-fold decrease and a 3-fold increase, respectively, in $k_{pol}/K_{d,dCTP}$ for dCTP insertion opposite G with Mg^{2+} when compared with wild type, substantially attenuated by substitution with Mn^{2+}. Crystal structures of pol ι ternary complexes, including the primer terminus 3′-OH and a non-hydrolyzable dCTP analogue opposite G with the active-site Mg^{2+} or Mn^{2+}, revealed that Mn^{2+} achieves more optimal octahedral coordination geometry than Mg^{2+}, with lower values in average coordination distance geometry in the catalytic metal A-site. Crystal structures of R96G revealed the loss of three H-bonds of residues Gly-96 and Tyr-93 with an incoming dNTP, due to the lack of an arginine, as well as a destabilized Tyr-93 side chain secondary to the loss of a cation-π interaction between both side chains. These results provide a mechanistic basis for alteration in pol ι catalytic function with coordinating metals and genetic variation.

Genomic DNA is continuously attacked by a variety of endogenous and exogenous agents in cells, and the persistent unrepaired lesions can lead to genomic mutations and related diseases such as cancer. DNA polymerases (pols),[2] as well as DNA repair enzymes, are key enzymes for maintaining or altering genomic integrity against DNA lesions during various DNA transactions in organisms. The DNA replicative mechanisms linked to DNA damage and repair are believed to contribute to producing various mutational signatures in human cancer genomes (1). At least 17 different human DNA polymerases have been identified to date, which differ in their functions in DNA replication, repair, recombination, and damage tolerance (2, 3).

Y-family DNA polymerases, including pols η, ι, κ, and REV1, are specialized in replicating through DNA lesions, so-called translesion DNA synthesis (TLS). These polymerases have low fidelity with undamaged DNA templates but have spacious and solvent-accessible active sites to allow the accommodation and replicative bypass of bulky and distorted DNA lesions (4). Individual Y-family polymerases play error-free or error-prone roles in TLS, depending on DNA lesion types in cells (5). At bulky carcinogen-derived N^2-G DNA lesions (e.g. benzo[a]pyrene-diol epoxide-G), both pol κ and REV1 catalyze error-free TLS, but both pols η and ι catalyze error-prone TLS (6–14). By contrast, at UV-induced cyclobutane thymine dimers (T-T), only pol η (but not the other Y-family pols) can catalyze error-free TLS (15, 16). Therefore, the overall balance toward error-free TLS with all working polymerases at various DNA lesions might be crucial in preventing mutations from numerous genotoxic agents. Recently, we reported that catalytic (either hypoactive or hyperactive) alterations are found in a considerable number of human germline non-synonymous variants of Y-family pols κ, ι, and REV1 (17–19), which might potentially influence on the overall TLS capacity in the affected individuals.

pol ι is exceptionally error-prone in DNA synthesis among polymerases, particularly opposite template bases G and T, due to its uniquely restricted active-site and related non-Watson-Crick base pairing (20–22). pol ι is able to catalyze nucleotide insertion opposite a variety of DNA lesions, including N^2- and O^6-alkyl and aralkyl G adducts, 8-oxo-7,8-dihydroG (8-oxoG),

TABLE 1
Pre-steady-state kinetic parameters for dCTP incorporation opposite G by pol ι(1– 445), pol ι(26 – 445), and R96G pol ι(1– 445) in the presence of either Mg^{2+} or Mn^{2+}

Metal	pol	k_{pol}	$K_{d,dCTP}$	$k_{pol}/K_{d,dCTP}$	Relative efficiency[a]
		s^{-1}	μM	$M^{-1} s^{-1}$	
$MgCl_2$ (2 mM)	pol ι (1–445)	0.43 ± 0.02	670 ± 100	6.4×10^2	1
	pol ι (26–445)	0.77 ± 0.024	390 ± 40	2.0×10^3	3.1
	R96G pol ι (1–445)	0.063 ± 0.007	5200 ± 1300	1.2×10	0.019
$MnCl_2$ (150 μM)	pol ι (1–445)	0.74 ± 0.06	1.5 ± 0.4	4.9×10^5	1
	pol ι (26–445)	0.79 ± 0.03	1.8 ± 0.2	4.4×10^5	0.90
	R96G pol ι (1–445)	0.077 ± 0.002	1.4 ± 0.1	5.5×10^4	0.11

[a] Relative efficiency, calculated as the ratio of the $k_{pol}/K_{d,dCTP}$ of each pol ι for dCTP insertion opposite G to the $k_{pol}/K_{d,dCTP}$ of pol ι(1– 445) for dCTP insertion opposite G.

pyrimidine dimers, and abasic sites, but mediates largely miscoding TLS (albeit occasionally accurate) with varied nucleotide selectivity depending on lesion type (13, 23, 24). Both C and T are inserted opposite template N^2- and O^6-alkyl and aralkyl G adducts by pol ι (13, 25). C is only slightly favored over G opposite template 8-oxoG by pol ι, A is favored opposite the 3′ T of (6-4) T-T photoproducts, and both G and T are favored opposite 5′ T of (6-4) T-T photoproducts and abasic sites (23, 24). A possible implication of pol ι in mutation and cancer has been suggested by substantial evidence from several knock-out mouse studies (26 –28), as well as from multiple studies verifying frequent pol ι dysregulation in various types of human cancers (29 –32). In this respect, the appropriate catalytic function of pol ι in cells might be required for preventing cancer. One of the distinctive catalytic properties of pol ι is the metal ion preference. Unlike other Y-family polymerases, pol ι is known to prefer Mn^{2+} over Mg^{2+} as the metal ion cofactor for catalysis (33, 34), but the structural mechanistic details remain speculative. In addition, substantial alterations were reported in metal-dependent DNA polymerase activity from two rare human germline pol ι variants, i.e. severe impairment of both Mg^{2+}-dependent and Mn^{2+}-dependent activities in the R96G variant and moderate enhancement of only the Mg^{2+}-dependent activity in the Δ1–25 variant for matched and mismatched nucleotide incorporations opposite normal and lesion templates (17). Detailed structural and kinetic mechanisms of catalytic alterations of pol ι by these genetic variants still remain unclear. Any disease associations have not been reported yet, but the catalytically altered pol ι genetic variants might be of potential importance in that they would change the TLS capacity of pol ι and consequently modify mutation phenotypes to genotoxic agents in genetically predisposed individuals.

To elucidate both the kinetic and the structural basis for alterations in the catalytic function of pol ι by different two metal ions, Mg^{2+} and Mn^{2+}, as well as by two human germline non-synonymous variants, R96G and Δ1–25, we performed pre-steady-state kinetic analysis for nucleotide insertion by pol ι and also determined x-ray crystal structures of ternary pol ι complexes in the presence of either Mg^{2+} or Mn^{2+} ions, using the recombinant human pol ι core (residues 1– 445) proteins of wild type and two variants with a simple model of a correct dCTP incorporation opposite normal G. The combined pre-steady-state kinetic and structural results indicate that Mn^{2+} enables pol ι to adopt more ideal octahedral coordination in the active site and achieve much higher catalytic efficiency than Mg^{2+}, whereas the R96G variant results in the loss of hydrogen

bond interactions of residues Gly-96 and Tyr-93 with an incoming nucleotide as well as conferring a much greater reduction in its catalytic efficiency. Our detailed kinetic and structural results are discussed in the context of understanding the possible mechanistic and functional aspects of metal ions and genetic variations on pol ι.

Results

Pre-steady-state Kinetic Analysis of dCTP Incorporation Opposite G by pol ι(1– 445), pol ι(26 – 445), and R96G pol ι(1– 445) Enzymes in the Presence of Mg^{2+} or Mn^{2+}—Pre-steady-state kinetic methods were used to quantify the alterations in catalytic efficiency and the apparent nucleotide binding affinity of pol ι by metal ions (Mg^{2+} or Mn^{2+}) and known human genetic variants (Δ1–25 or R96G). Pre-steady-state kinetic parameters were determined for dCTP incorporation opposite template G into 18-mer/36-mer duplexes by pol ι(1–445), pol ι(26 – 445), and R96G pol ι(1– 445) enzymes under single turnover conditions (where pol ι was present in 10-fold excess over DNA substrate), in the presence of either 0.15 mM $MnCl_2$ or 2 mM $MgCl_2$, which is in the optimal range for pol ι activity (33, 34), using a rapid quench flow instrument. Analysis of the change of the observed rate (k_{obs}) as a function of increasing dCTP concentration yielded k_{pol}, the maximal rate of nucleotide incorporation, and $K_{d,dCTP}$, a measure of the binding affinity of dCTP to the pol·DNA binary complex to form a ternary complex poised for catalysis (Table 1 and supplemental Fig. S1). pol ι(1– 445) displayed a k_{pol} of 0.74 ± 0.06 s^{-1} and a $K_{d,dCTP}$ of 1.5 ± 0.4 μM in the presence of Mn^{2+}. Thus, the catalytic efficiency ($k_{pol}/K_{d,dCTP}$) of pol ι(1– 445) with Mn^{2+} was estimated to be 4.9×10^5 M^{-1} s^{-1}, which was 770-fold higher than that with Mg^{2+}, mainly due to a 450-fold lower $K_{d,dCTP}$. Similar trends of kinetic results were also observed with pol ι(26 – 445) and the R96G variant, indicating that pol ι binds nucleotide much more tightly and catalyzes nucleotide insertion much more efficiently in the presence of Mn^{2+} than in the presence of Mg^{2+}. pol ι(26 – 445) had a $k_{pol}/K_{d,dCTP}$ value similar to that of pol ι(1– 445) in the presence of Mn^{2+} but displayed a 3-fold increase in $k_{pol}/K_{d,dCTP}$ in the presence of Mg^{2+} when compared with pol ι(1– 445), indicating a slight enhancement only in the Mg^{2+}-dependent catalytic efficiency of pol ι due to the deletion of N-terminal 25 residues. The R96G variant showed a 53-fold decrease in $k_{pol}/K_{d,dCTP}$ for dCTP insertion opposite G in the presence of Mg^{2+} when compared with that with wild type, while showing a 9-fold decrease of that value in the presence of Mn^{2+}. This mitigation effect of Mn^{2+} on the Mg^{2+}-de-

TABLE 2
Crystal data, data collection parameters, and structure refinement statistics

	Complex					
	pol ι(26−445) G·dCMPNPP (Mg²⁺)	pol ι(26−445) G·dCMPNPP (Mn²⁺)	pol ι(1−445) G·dCMPNPP (Mg²⁺)	pol ι(1−445) G·dCMPNPP (Mn²⁺)	R96G pol ι(1−445) G·dCMPNPP (Mg²⁺)	R96G pol ι(1−445) G·dCMPNPP (Mn²⁺)
Data collection						
Wavelength (Å)	0.97872	0.97872	0.97872	0.97872	0.97872	0.97872
Space group	$P6_522$	$P6_522$	$P6_522$	$P6_522$	$P6_522$	$P6_522$
Resolution (Å)[a]	50.00−2.49 (2.53−2.49)	50.00−2.64 (2.69−2.64)	50.00−3.56 (3.62−3.56)	50.00−3.15 (3.20−3.15)	50.00−2.78 (2.83−2.78)	50.00−2.80 (2.85−2.80)
Unit cell (*a*, *b*, *c*) (Å)	97.61, 97.61, 203.00	97.83, 97.83, 202.89	98.27, 98.27, 201.66	97.74, 97.74, 202.01	98.12, 98.12, 202.72	97.54, 97.54, 202.21
Unit cell (α, β, γ) (°)	90.00, 90.00, 120.00	90.00, 90.00, 120.00	90.00, 90.00, 120.00	90.00, 90.00, 120.00	90.00, 90.00, 120.00	90.00, 90.00, 120.00
No. of unique reflections[a]	20,810 (1006)	17,727 (847)	7564 (363)	10,495 (487)	15,324 (729)	14,993 (720)
Completeness (%)[a]	99.6 (99.4)	100 (100)	99.9 (100)	99.8 (99.6)	100 (100)	99.9 (99.9)
$I/\sigma(I)$[a]	36.2 (3.5)	31.8 (4.0)	11.6 (2.5)	22.9 (4.5)	30.4 (2.8)	30.1 (3.7)
Wilson *B*-factor (Å²)	32.2	33.7	62.1	40.0	46.7	41.9
R_{merge}[a,b]	0.121 (0.914)	0.090 (0.784)	0.222 (0.990)	0.180 (0.811)	0.100 (0.922)	0.117 (0.842)
Redundancy[a]	21.3 (22.0)	21.2 (21.8)	14.9 (14.4)	20.8 (21.1)	17.7 (17.4)	21.0 (21.3)
Refinement						
R_{work}	0.220	0.204	0.204	0.202	0.217	0.224
R_{free}	0.249	0.248	0.244	0.236	0.250	0.266
No. of atoms						
Protein/DNA	2941/345	2934/345	2928/329	2926/345	2890/345	2887/345
dNTP/Metal ions	28/3[c]	28/3[c]	28/2	28/2	28/1	28/2
Water	85	65	0	0	22	10
B-factor (Å²)						
Average	53.9	51.6	68.9	46.4	65.0	51.4
Protein/DNA	54.9/50.4	52.5/47.3	69.5/64.9	47.2/41.0	65.4/63.9	51.9/49.6
dNTP/Metal ions	34.9/36.7	32.4/59.0	54.3/44.9	26.3/43.9	47.8/40.7	31.6/30.6
Water	42.6	41.1	−	−	48.7	34.1
Root mean square deviations						
Bonds (Å)	0.005	0.009	0.003	0.004	0.003	0.003
Angles (°)	0.886	1.024	0.633	0.676	0.653	0.629
Ramachandran						
Favored (%)	98.7	97.9	97.1	97.3	98.4	97.6
Allowed (%)	1.1	1.9	2.9	2.7	1.6	2.4
Outliers (%)	0.3	0.3	0.0	0.0	0.0	0.0
PDB code	**5KT2**	**5KT3**	**5KT6**	**5KT7**	**5KT4**	**5KT5**

[a] Values for highest resolution shell are given in parentheses.
[b] R_{merge}: $R_{linear} = \text{SUM}(\text{ABS}(I - \langle I \rangle))/\text{SUM}(I)$, where I is the integrated intensity of a given reflection.
[c] One non-catalytic metal ion is present in the structure.

pendent $k_{pol}/K_{d,dCTP}$ reduction in the R96G variant seemed to be mainly due to the full restoration of the apparent dCTP binding affinity to the level comparable with that of wild type by Mn^{2+}.

Crystal Structures of Human pol ι Pre-catalytic Ternary Complexes Incorporating Nonhydrolyzable dCTP Analogue (dCMPNPP) Opposite Template G in the Presence of Mg²⁺ or Mn²⁺—To observe the structural alterations of pol ι by metal ions (Mg²⁺ or Mn²⁺) and genetic variants (Δ1−25 or R96G), we determined six crystal structures of pre-insertion ternary complexes of pol ι(1−445), pol ι(26−445), and R96G pol ι(1−445) with DNA containing template G and dCMPNPP in the presence of either Mg²⁺ or Mn²⁺. The strategy, employing a nonhydrolyzable dCTP analogue, dCMPNPP, as well as DNA substrate having an intact 3′-OH at the primer end, was utilized to capture pre-catalytic ternary pol ι complexes that preserve metal-coordinating ligands in the active site while preventing catalysis in the presence of active-site metal ions, as successfully applied with pol β (35). Crystals of ternary complexes of pol ι(26−445), pol ι(1−445), and R96G pol ι(1−445) diffracted to about 2.5−2.6, 3.2−3.6, and 2.8 Å resolution, respectively (Table 2). All ternary complex structures of pol ι contained two metal ions with relatively lower occupancy in the A-site metal ions in the active site, except for the R96G pol ι(1−445)·Mg²⁺ ternary complex that missed an Mg²⁺ ion at the metal A-site near the primer terminus 3′-OH. To our knowledge, our structures represent the first ternary pol ι structures containing the primer end 3′-OH entity, as well as defining the position of two active-site metal ions of either Mg²⁺ or Mn²⁺, which provides geo-

metric information in the pre-catalytic state. However, electron density was not observed for the N-terminal 25 residues in all pol ι(1−445) ternary complexes, suggesting the disordered nature of this negatively charged N-terminal region. Thus, all the refined structures of pol ι ternary complexes contained pol ι residues 51−439 as observed previously with the ternary pol ι(26−445) complex structure (36). The overall structures of six ternary pol ι complexes were almost identical, except for subtle variations near metal ions in the active site and at the amino acid substitution site (supplemental Fig. S2). Three pol ι structures with the Mn²⁺ ions were superimposed with root mean square deviations (RMSD) of 0.20−0.27 Å among the positions of Cα atoms (supplemental Fig. S2, *A and B*), whereas three pol ι structures with Mg²⁺ ions were superimposed with RMSD of 0.31−0.35 Å, indicating slightly more backbone variations in the presence of Mg²⁺ (supplemental Fig. S2, *A–D*). Superposition of relatively high resolution (2.5 and 2.6 Å, respectively) structures of the pol ι(26−445)·Mg²⁺ and pol ι(26−445)·Mn²⁺ ternary complexes showed almost identical overall structures between them with an RMSD of 0.20 Å over Cα atoms but displayed slight differences in positions of metal ions as well as side chains of nearby residues Asp-59 and Glu-152 in the active site (Fig. 1*B*), indicating possible differences between Mg²⁺ and Mn²⁺ coordination in the pol ι active site.

Coordination of Two Divalent Mg²⁺ or Mn²⁺ Ions in the Active Sites of Human pol ι(26−445) Ternary Complexes with Primer 3′-OH and dCMPNPP—To understand the differences in the metal coordination geometry between Mg²⁺ and Mn²⁺ ions in the pol ι active site, we compared the coordination
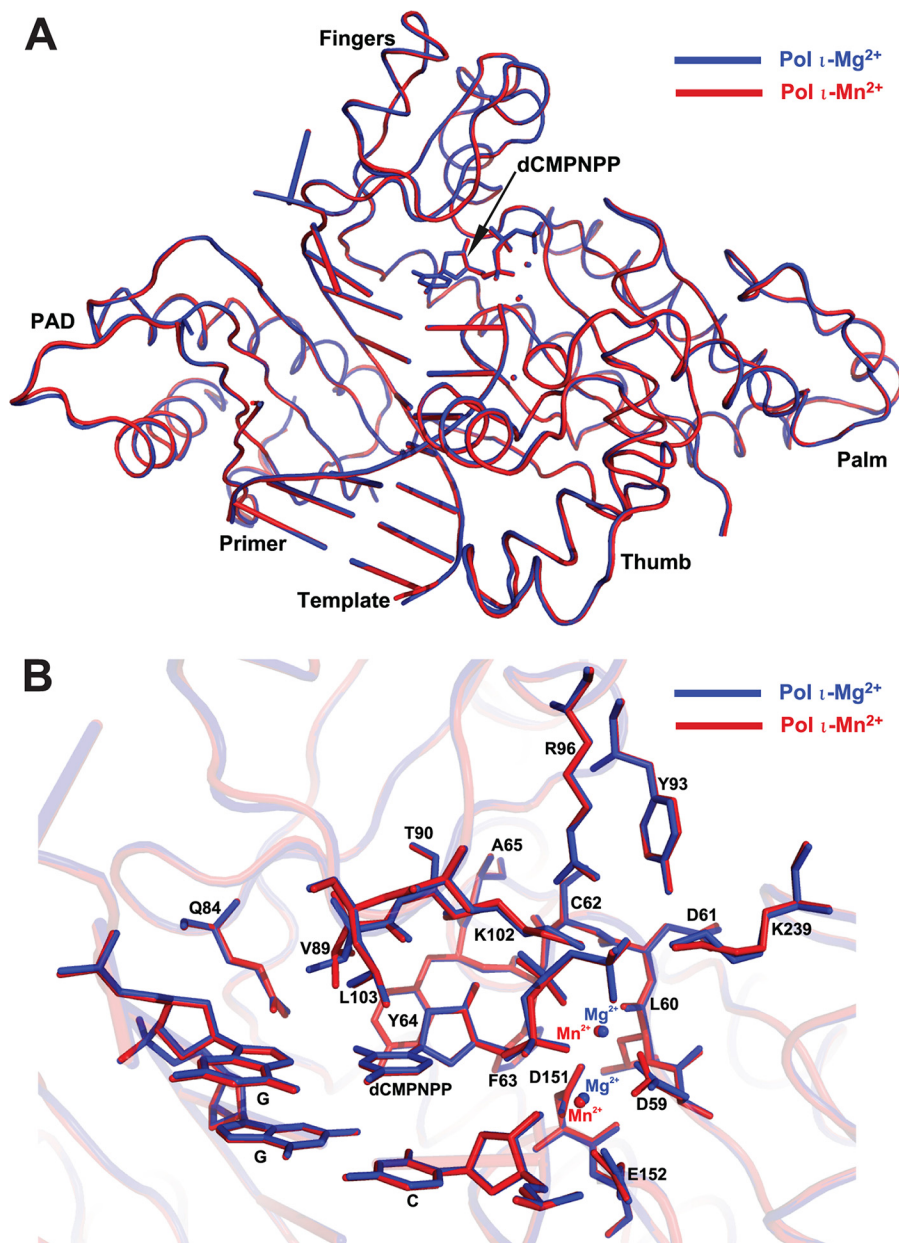
FIGURE 1. **Structures of pol ι·DNA·nucleotide ternary complexes in the presence of Mg^{2+} or Mn^{2+}.** *A*, superposition of the overall structures of ternary complexes of pol ι(26–445) with DNA containing template G and incoming non-hydrolyzable dCMPNPP in the presence of Mg^{2+} (*blue*) or Mn^{2+} (*red*). pol ι is shown as ribbons, DNA is shown as tube and ladder, the nucleotide is shown as sticks, and metal ions are shown as spheres. *B*, superposition of the active sites of the pol ι(26–445)·G·dCMPNPP·Mg^{2+} (*blue*) and pol ι(26–445)·G·dCMPNPP·Mn^{2+} (*red*) complexes. Active-site residues, DNA, and nucleotide are shown as sticks, and metal ions are shown as spheres.

structures of Mg^{2+} and Mn^{2+} ions in the pol ι active site utilizing relatively high resolution structures of the pol ι(26–445)·Mg^{2+} and pol ι(26–445)·Mn^{2+} ternary complexes. The $F_o - F_c$ omit maps for the incoming nucleotide and metal ions showed clear density for the incoming dCMPNPP and two Mg^{2+} (or Mn^{2+}) ions bound in the pol ι active site (Fig. 2, *A* and *B*). Two Mg^{2+} or Mn^{2+} ions were present in both the catalytic metal site (A-site) and the nucleotide binding metal site (B-site) in the pol ι active site, as typically observed with polymerases (37), although having partial occupancies (63 and 67%, respectively) at the A-site. Both Mg^{2+} and Mn^{2+} at the B-site in the pol ι active site showed nearly perfect octahedral coordination geometry with six ligands, which had similar values of average

coordination distance (2.14 and 2.06 Å, respectively) and distance RMSD (0.230 and 0.214 Å, respectively), albeit slightly lower with Mn^{2+} (Table 3 and Fig. 2, *C–E*), as observed with the B-site Mg^{2+} in the previously reported structures of normal G·dCMPNPP ternary complexes of pols β and η (38, 39). The A-site Mn^{2+} in the pol ι ternary complex also showed good octahedral coordination geometry involving five ligands, although missing one ligand (possibly a water molecule observed with pols β and η ternary complexes) (38, 39), yielding average coordination distance (2.29 Å) and distance RMSD (0.305 Å) values that were similar to those (2.22–2.34 and 0.187–0.293 Å, respectively) observed with the A-site Mg^{2+} in the normal G·dCMPNPP ternary complexes of pols β and η (38,
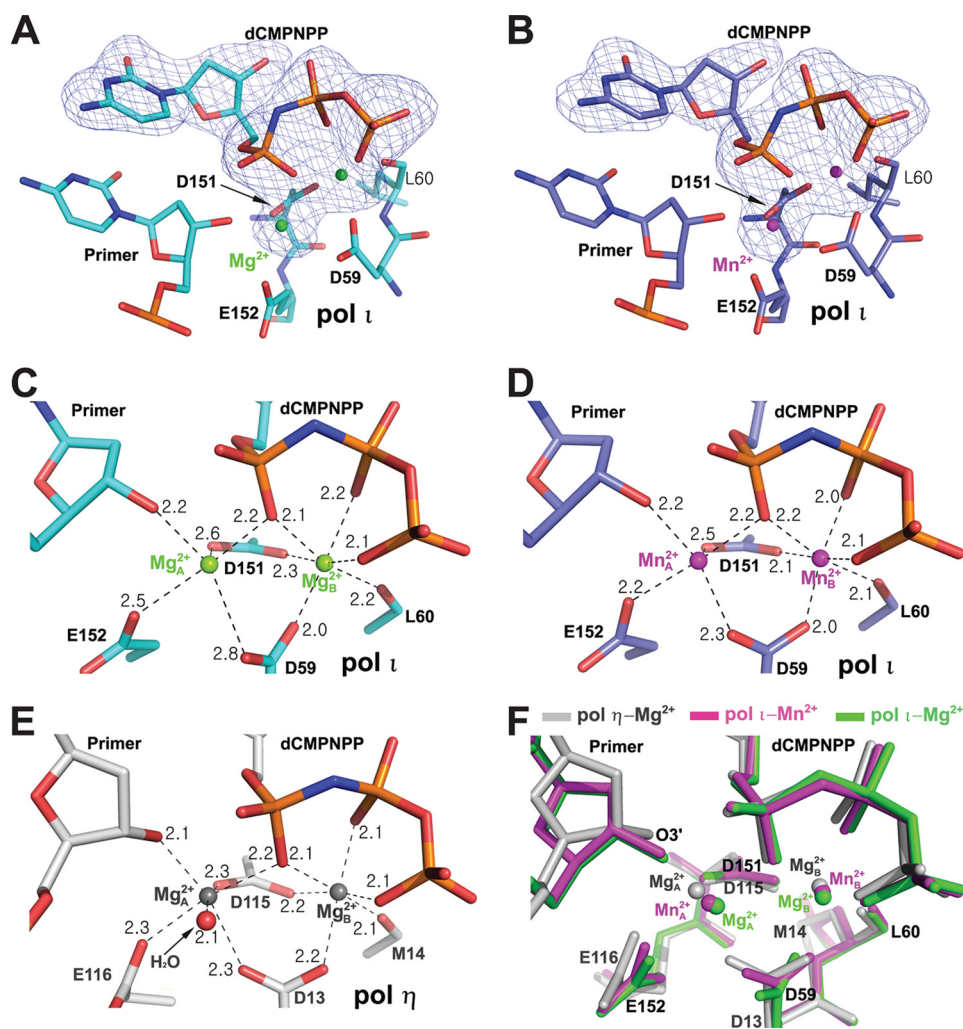
FIGURE 2. **Comparison of Mg²⁺ and Mn²⁺ coordinations in the pol ι active site.** *A* and *B*, $F_o - F_c$ simulated annealing omit maps (*blue*) contoured at 3.0σ for the incoming dCMPNPP and Mg²⁺ (*A*) or Mn²⁺ (*B*) ions in the active sites of pol ι. The electron density is superimposed on the refined modeled dCMPNPP and metal ions. Mg²⁺ and Mn²⁺ ions are shown as *green* and *magenta spheres*, respectively. *C* and *D*, close-up view of Mg²⁺ (*C*) or Mn²⁺ (*D*) coordination in the active-site metal binding sites of pol ι·G·dCMPNPP complexes. Metal ion coordination is shown as *dashed lines*, and the coordination distances are indicated. *E*, close-up view of Mg²⁺ coordination in the active-site metal binding site of pol η·G·dCMPNPP complex (PDB ID 4DL3). Mg²⁺ ions are shown as *gray spheres*. *F*, superposition of the active-site metal binding sites of the pol ι(26–445)·G·dCMPNPP·Mg²⁺ (*green*), pol ι(26–445)·G·dCMPNPP·Mn²⁺ (*magenta*), and pol η·G·dCMPNPP·Mg²⁺ (PDB ID 4DL3, *gray*) complexes. *Red, blue,* and *orange* colors indicate oxygen, nitrogen, and phosphorus atoms, respectively. *Cyan* (in *A* and *C*), *light blue* (in *B* and *D*), and *light gray* (in *E*) colors indicate carbon atoms.

TABLE 3

Active site metal coordination distances and angles in normal G·dCMPNPP ternary complex structures of pols ι, η, and β in the presence of divalent metal ions

pol	Metal ion	Inter-metal distance	A-site metal coordination			B-site metal coordination		
			n^a	Distance^b (Å)	Distance RMSD^c (Å)	n	Distance (Å)	Distance RMSD (Å)
pol ι(26–445)	Mg²⁺	3.23	5	2.45 ± 0.12	0.474	6	2.14 ± 0.04	0.230
	Mn²⁺	3.43	5	2.29 ± 0.06	0.305	6	2.06 ± 0.04	0.214
pol ι(1–445)	Mg²⁺	3.02	5	2.37 ± 0.14	0.869	6	2.13 ± 0.05	0.257
	Mn²⁺	3.33	5	2.22 ± 0.18	0.409	6	2.10 ± 0.07	0.336
pol η^d	Mg²⁺	3.55	6	2.34 ± 0.06	0.256	6	2.17 ± 0.04	0.236
pol η^e	Mg²⁺	3.72	6	2.22 ± 0.04	0.187	6	2.13 ± 0.03	0.215
pol β^f	Mg²⁺	3.44	6	2.23 ± 0.06	0.293	6	2.04 ± 0.02	0.183

[a] Coordination number.
[b] Average coordination distance ± standard error.
[c] Distance RMSD from the ideal octahedral geometry was estimated by UCSF Chimera (56).
[d] PDB ID 4DL2 (38).
[e] PDB ID 4DL3 (38).
[f] PDB ID 4TUQ (39).

39) (Table 3 and Fig. 2, *D* and *E*). In strong contrast, the Mg²⁺ at the A-site in the pol ι active site showed a considerable deviation from the ideal octahedral coordination geometry, yielding

average coordination distance (2.45 Å) and distance RMSD (0.474 Å) values that were substantially higher than those with Mn²⁺ (Table 3 and Fig. 2, *C* and *D*). These more optimal fea-
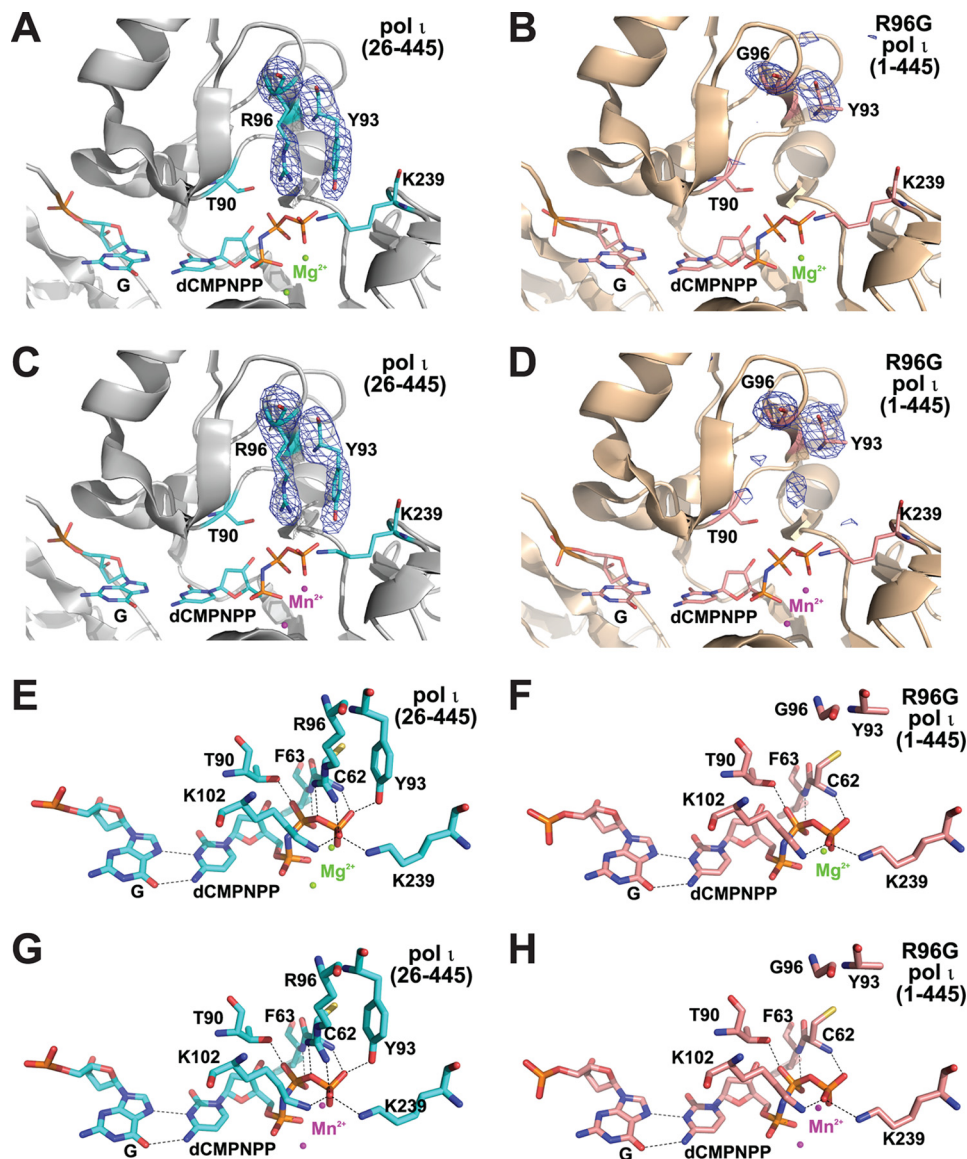
FIGURE 3. **The active sites of R96G pol ι ternary complexes in the presence of Mg^{2+} or Mn^{2+}.** *A–D*, $F_o − F_c$ simulated annealing omit maps contoured at 3.0σ for the residues Arg-96 (or Gly-96) and Tyr-93 in the active sites of pol ι(26–445)·G·dCMPNPP·Mg^{2+} (*A*); R96G pol ι(1–445)·G·dCMPNPP·Mg^{2+} (*B*); pol ι(26–445)·G·dCMPNPP·Mn^{2+} (*C*); and R96G pol ι(1–445)·G·dCMPNPP·Mn^{2+} (*D*) complexes. The electron density (*blue mesh*) is superimposed on the refined modeled residues Arg-96 (or Gly-96) and Tyr-93. Mg^{2+} and Mn^{2+} ions are shown as *green* and *magenta spheres*. *E–H*, close-up view of the active sites of pol ι(26–445)·G·dCMPNPP·Mg^{2+} (*D*); R96G pol ι(1–445)·G·dCMPNPP·Mg^{2+} (*F*); pol ι(26–445)·G·dCMPNPP·Mn^{2+} (*G*); and R96G pol ι(1–445)·G·dCMPNPP·Mn^{2+} (*H*) complexes. Hydrogen-bonding interactions are shown as *dashed lines*. *Red, blue, orange,* and *yellow* colors indicate oxygen, nitrogen, phosphorus, and sulfur atoms, respectively. *Cyan* (in *A, C, E,* and *G*) and *light pink* (in *B, D, F,* and *H*) colors indicate carbon atoms.

tures with Mn^{2+} than Mg^{2+} for octahedral coordination geometry at the A-site were similarly observed with the refined pol ι(1–445) ternary complex structures (Table 3), albeit having lower resolution (3.6 and 3.2 Å). The poor coordination with Mg^{2+} at the A-site appeared to be related to subtle displacement of the side-chain carboxyl group of Asp-59 away from the A-site Mg^{2+} as well as a slight shift of the A-site Mg^{2+} to the B-site Mg^{2+}, yielding a 0.2 Å shortening of inter-metal distance when compared with that with Mn^{2+} in the pol ι active site (Fig. 2, *C*, *D*, and *F*). Interestingly, the C3′-endo conformation was equally observed at the sugar moieties at the 3′ primer end (Fig. 2), as well as the nucleotide 5′ to the primer end, and three nucleotide pairs at positions *n*-2 to *n*-4 of the primer/template duplex in both pol ι ternary complex structures, unlike the pre-

viously reported structures of the pol ι binary and ternary complexes lacking the primer end 3′-OH (Protein Data Bank (PDB) IDs 2FLP and 2ALZ) (36, 40), indicating a distinctive pattern of sugar pucker changes induced in the pre-catalytic pol ι ternary complex.

Active-site Structures of Human R96G pol ι(1–445) Ternary Complexes in the Presence of Mg^{2+} or Mn^{2+}—To reveal the structural mechanism of severe catalytic impairments in the R96G pol ι variant, we compared the active-site structures of R96G pol ι(1–445) ternary complexes with those of pol ι(26–445) ternary complexes of relatively high resolution. Interestingly, the R96G variant structures showed substantial alterations not only at the amino acid substitution site (Gly-96) but also at the nearby residue site (Tyr-93), when compared with

pol ι(26 – 445) (Fig. 3). The $F_o - F_c$ simulated annealing omit maps for two key residues (Gly-96 and Tyr-93) in R96G pol ι·Mg^{2+} and R96G pol ι·Mn^{2+} ternary complexes showed no clear electron density for two long side chains of Arg-96 and Tyr-93 (Fig. 3, *B* and *D*), which were obviously observed in those with the pol ι(26 – 445) complexes (Fig. 3, *A* and *C*). This collateral destabilization of the Tyr-93 side chain seems to be related to the loss of a cation-π interaction between Arg and Tyr side chains due to the loss of an Arg side chain in the R96G variant. Accordingly, two hydrogen bonds of the Arg-96 side chain with a β,γ-bridging oxygen and a γ-phosphate oxygen of dCMPNPP, as well as one hydrogen bond of the Tyr-93 side chain with a γ-phosphate oxygen, were lost in R96G variant structures when compared with those in pol ι(26 – 445) ternary complex structures (Fig. 3, *E–H*). Interestingly, only Mn^{2+} but not Mg^{2+} was observed at the A-site in the R96G pol ι active site (Fig. 3, *B* and *D*), possibly reflecting an inferior A-site binding ability of Mg^{2+} when compared with Mn^{2+}, which might in part be attributed to a 6-fold greater decrease in catalytic efficiency of the R96G variant with Mg^{2+} than that with Mn^{2+} (Table 1).

Discussion

In this study, we provide structural and pre-steady-state kinetic evidence that Mn^{2+} is more optimal for the two-metal ion binding site configuration and catalysis of pol ι than Mg^{2+}. Our pol ι ternary complex structures containing intact coordinating ligands such as the primer end 3′-OH reveal that Mn^{2+} ions achieve more ideal octahedral coordination geometry than Mg^{2+} ions in the pol ι active site, specifically in the catalytic metal A-site. Moreover, our pre-steady-state kinetic data demonstrate that Mn^{2+} ions confer much higher (2–3 orders of magnitude) efficiency of pol ι catalysis than Mg^{2+} ions, mainly through augmenting nucleotide binding affinity. We also confirmed that the R96G variant, displaying a severe reduction in catalytic efficiency, loses three hydrogen bond interactions of two residues (Gly-96 and Tyr-93) with an incoming nucleotide in the pol ι active site. Interestingly, Mn^{2+} substantially rescued the catalytic impairment in the Gly-96 variant by restoring the apparent nucleotide binding affinity. The Δ1−25 variant displayed a small alteration (3-fold increase) only in Mg^{2+}-dependent catalytic efficiency, although the structural effects of N-terminal 25 residues are not discernible due to the absence of their electron density.

The key differences between the pol ι(26 – 445)·Mg^{2+} and pol ι(26 – 445)·Mn^{2+} ternary complex structures were located at and near the catalytic metal A-site in the pol ι active site, particularly the configuration of the Asp-59 side chain as well as the positioning of the A-site metal (Fig. 2*F*), which substantially modified the A-site metal coordination. First, in the presence of Mg^{2+} ions as opposed to Mn^{2+} ions, the side-chain carboxyl group of Asp-59 is rotationally displaced to locate a ligand atom (one carboxyl oxygen of Asp-59) more distant (0.5 Å) from the A-site metal (despite no alteration in coordination distance between the other carboxyl oxygen and the B-site metal) in the pol ι active site. Second, Mg^{2+} (when compared with Mn^{2+}) at the A-site was positionally shifted closer (~0.2 Å) to the B-site metal in the pol ι active site, yielding an inter-metal distance

shorter than that with Mn^{2+} ions (Table 3). Thus, in the pol ι active site, only Mn^{2+} ions but not Mg^{2+} ions seem to achieve an inter-metal distance similar to that with Mg^{2+} ions usually observed in active sites of ternary complex structures of other human pols η and β with normal G·dCMPNPP (38, 39) (Table 3). Superposition of the active-site metal binding sites of pol ι·Mg^{2+}, pol ι·Mn^{2+}, and pol η·Mg^{2+} (PDB ID 4DL3) ternary complexes appears to reflect some gradational changes in the extent of positional shift of the A-site metal (toward the B-site metal) as well as in the angle of rotational displacement of the side-chain carboxyl group of Asp-59 (or Asp-13 for pol η), in the order of pol η·Mg^{2+} < pol ι·Mn^{2+} < pol ι·Mg^{2+}. (Fig. 2*F*). Consequently, Mg^{2+} ions led to a considerable deviation from the ideal octahedral coordination geometry at the A-site, yielding the values of average coordination distance and distance RMSD (2.45 and 0.474 Å, respectively), which were quite higher than those with Mn^{2+} (Table 3). These coordination parameters with Mg^{2+} ions seem to be slightly improved in the aspect of average coordination distance but worsened in the aspect of distance RMSD by the presence of the primer terminus 3′-OH, when compared with those (2.66 and 0.456 Å, respectively) of the A-site Mg^{2+} (albeit involving only four coordinating atoms) in the previously reported structure (PDB ID 2ALZ) of pol ι ternary complex lacking the primer end 3′-OH (36). This Mg^{2+}-induced geometric alteration at the A-site in the pol ι active site contrasts with the near perfect octahedral coordination of the A-site Mg^{2+} observed in ternary complex structures of other pols η and β with the correct incoming non-hydrolyzable nucleotide (Table 3) (38, 39).

The Mn^{2+} requirement for achieving the optimal octahedral coordination geometry at the A-site in ternary complex structures with the correct incoming nucleotide seems to be unique in pol ι. Other DNA polymerases such as bacteriophage pol RB69 and human pol β achieve good octahedral coordination geometry not only with Mg^{2+} but also with Mn^{2+} at the A-site, as observed in their ternary complex structures with the correct incoming non-hydrolyzable nucleotide (PDB IDs 3SJJ, 3SPY, 2FMS, and 3C2K) (35, 41, 42). It is notable that the superior coordinating ability of Mn^{2+} when compared with Mg^{2+} at the A-site is observed in the previously reported structures of ternary pol β complexes (PDB IDs 4PGQ, 4PGX, 4PHA, and 4PHD) with an incoming incorrect non-hydrolyzable nucleotide (43). Our data and that of others suggest that Mn^{2+} is more tolerant of atypical pol active sites (*e.g.* the inherently restricted pol ι active site and the distorted pol active site due to base pair mismatch) than Mg^{2+}) and thus able to form good octahedral coordination geometry not only at the B-site but also at the A-site in the pol active site. This effect might be attributed to a relaxed coordination requirement of Mn^{2+} when compared with Mg^{2+} (37). It is of interest to perform further studies to verify whether our results of pol ι with normal base pairs of template G and incoming dCTP are valid for other base pairs involving DNA lesions or mismatches such as G:T and T:G pairs.

The Mg^{2+}-induced distortion of the A-site coordination geometry in the pol ι active-site structure seems to be closely related to a severe (220 – 770-fold) diminution in catalytic efficiency ($k_{pol}/K_{d,dCTP}$) of pol ι in the presence of Mg^{2+} when

compared with Mn^{2+} (Table 1). This severe catalytic impairment with Mg^{2+} was mainly due to a severe reduction in the affinity of productive nucleotide binding of pol ι in the presence of Mg^{2+} when compared with Mn^{2+}, as reflected by large (220–450-fold) increases in the apparent equilibrium dissociation constant ($K_{d,dCTP}$) for incoming dCTP (Table 1). These results suggest that substitution of Mn^{2+} for Mg^{2+} might boost the catalytic efficiency of pol ι for correct nucleotide insertion, mainly through improving the binding affinity of nucleotide, by achieving optimal octahedral coordination at the A-site in the active site. Our finding is in good agreement with previous studies with other polymerases, *e.g.* RB69 and pol β (42, 44). It is also notable that the extent of increases (220–450-fold) in the nucleotide binding affinity by Mn^{2+} substitution appears to be much higher with pol ι (Table 3) than those (3–4- and 8–19-fold, respectively) observed with RB69 and pol β (42, 44), implying a more marked effect of Mn^{2+} on pol ι than other polymerases. Our combined structural and kinetic data suggest that the optimal octahedral coordination of two active-site metal ions is essential for proper catalytic function of pol ι, and Mn^{2+} is superior in this respect when compared with Mg^{2+}, particularly at the A-site in the pol ι active site. The superiority of Mn^{2+} for pol ι function is also supported by the biochemical property of pol ι(1–445) to more tightly bind DNA substrates in the presence of a low level of Mn^{2+} than Mg^{2+} (17). Although DNA polymerases most likely utilize physiologically abundant Mg^{2+} ions for catalysis *in vivo*, from our and previous studies (17, 33, 34), it may be relevant to postulate that pol ι would inherently employ physiologically low levels of Mn^{2+} for catalysis in kinetic and structural preference to Mg^{2+} *in vivo*. Similarly, pol λ has been also suggested to use Mn^{2+} as the preferred activating metal ion *in vivo* (45). Mn^{2+} has also been reported to increase the activity of non-canonical DNA polymerases such as *Sulfolobus solfataricus* Dpo4 and human Prim-Pol *in vitro* (46, 47). We also note a very recent study suggesting the requirement of a third metal ion for pol η catalysis, with slight preference for Mg^{2+} (48). It would be of interest to investigate whether this is the case in pol ι catalysis.

The loss of hydrogen-bonding interactions of two structurally altered residues, the substituted Gly-96 and the nearby destabilized Tyr-93, with the incoming nucleotide in the crystal structures of the R96G pol ι ternary complexes (Fig. 3) may provide a molecular explanation for severe diminution of the catalytic efficiency in the R96G variant (Table 1). The disordered electron density of the Tyr-93 side chain in R96G pol ι crystal structures seems to be related to the destabilization of the Tyr-93 side chain due to the absent cation-π interaction with Gly-96. Both Arg-96 and Tyr-93 residues, which are conserved and important residues for nucleotide binding in all Y-family pols (20), seem to co-stabilize their side chain conformations by forming the cation-π interaction between their parallel side chains as observed in our pol ι ternary complexes (Fig. 3). In good accordance with our data, individual missense mutations of two homologous Arg-67 and Tyr-64 residues in yeast pol η severely diminish its catalytic activity (49). It can be postulated that the weakened interaction of the R96G variant with incoming nucleotide likely diminishes its nucleotide binding affinity and catalytic efficiency. Interestingly, the attenuat-ing effect of the R96G variation on the apparent nucleotide binding affinity of pol ι was observed much more strongly in the presence of Mg^{2+} (Table 1). Mn^{2+} substitution fully restored the apparent nucleotide binding affinity of the R96G variant to a level similar to that of wild-type pol ι (Table 1), indicating a rescuing effect of Mn^{2+} to offset the destabilized nucleotide interaction in the R96G variant. Accordingly, the extent of reduction of catalytic efficiency in the R96G variant was considerably lessened in the presence of Mn^{2+} when compared with Mg^{2+} (Table 1).

The variant of pol ι(26–445) lacking the N-terminal 25 residues retained an Mn^{2+}-dependent catalytic efficiency almost similar to that of the pol ι(1–445) but displayed a 3-fold increase in selectivity in Mg^{2+}-dependent catalytic efficiency when compared with that of the pol ι(1–445) (Table 1). These results are in good agreement with our previous steady-state kinetic data (17). However, the structural effects of the N-terminal 25 residues are not clear due to their disordered nature in the x-ray crystal structure. Although it may not be obvious due to its low resolution (3.6 Å), interestingly, our refined crystal structure of pol ι(1–445) ternary complex in the presence of Mg^{2+} appeared to have slightly altered conformations of Arg-96 and Tyr-93 side chains when compared with the pol ι(26–445) ternary complex (supplemental Fig. S1C). This subtle structural alteration, observed only with Mg^{2+} ions in the pol ι(1–445) active site, may in part explain a slightly lower efficiency for Mg^{2+}-dependent catalysis by pol ι(1–445) when compared with pol ι(26–445).

In summary, we have investigated the effects of different metal ions (Mg^{2+} and Mn^{2+}) and genetic variations (R96G and Δ1–25) on both the structure and the catalytic function of pol ι. Here we report the first x-ray crystal structures acquired in the presence of either Mg^{2+} or Mn^{2+} of pol ι ternary complexes having intact coordinating metals and ligands such as the primer terminus 3'-OH. Comparisons of active-site conformations between pol ι·Mg^{2+} and pol ι·Mn^{2+} ternary complexes revealed that pol ι adopts near perfect octahedral coordination geometries for two metal ions in the active site only in the presence of Mn^{2+}. This structural feature with Mn^{2+} is clearly consistent with the pre-steady-state kinetic observation that Mn^{2+} greatly bolsters the apparent nucleotide binding affinity and the catalytic efficiency of pol ι when compared with observations with Mg^{2+}. Moreover, our combined structural and pre-steady-state kinetic analysis also revealed that the catalytic impairment in the R96G variant is related to the lack of hydrogen-bonding interactions of Gly-96 and Tyr-93 with incoming nucleotides in the active site. Our comparison between pol ι(1–445) and pol ι(26–445) also suggests a potential role of the disordered N-terminal 25 amino acids in selectively improving (albeit slightly) the Mn^{2+}-dependent catalytic efficiency in the wild-type pol ι. Overall, our study provides insights into the delicate structural and kinetic features of different metal coordination and genetic variants that contribute to understanding of the molecular basis of the catalytic function of pol ι.

Experimental Procedures

Materials—T4 polynucleotide kinase and dNTPs were purchased from New England Biolabs (Ipswich, MA). [γ-^{32}P]ATP

(specific activity 3×10^3 Ci/mmol) was from PerkinElmer Life Sciences. DNA oligonucleotides were from Sigma-Genosys. Micro Bio-Spin columns were from Bio-Rad. Protease inhibitor cocktail tablets were from Roche Applied Science. FPLC columns and PreScission protease were from GE Healthcare (Uppsala, Sweden). The wild-type, Δ1–25, and R96G variant forms of recombinant human pol ι core proteins (residues 1–445) were purified using previously described protocols (17). The nonhydrolyzable dCTP analogue dCMPNPP was from Jena Bioscience (Jena, Germany). Polyethylene glycol monomethyl ether 5000 was from Hampton Research (Aliso Viejo, CA).

Pre-steady-state Reactions—The 18-mer primer (5′-AGC CAG CCG CAG ACG CAG-3′) was 5′ end-labeled using T4 polynucleotide kinase with [γ-^{32}P]ATP and annealed with 36-mer template (3′-CGG AGC TCG GTC GGC GTC TGC GTC GCT CCT GCG GCT-5′). Rapid quench experiments were performed using a model RQF-3 KinTek Quench Flow instrument (KinTek Corp., Snow Shoe, PA). All DNA polymerase reactions were performed in 50 mM Tris-HCl (pH 7.5) buffer containing 5 mM dithiothreitol, 100 μg ml^{-1} BSA (w/v), 10% glycerol (v/v), and 2 mM MgCl$_2$ (or 0.15 mM MnCl$_2$). Reactions were initiated by rapid mixing of ^{32}P-primer/template/polymerase mixtures (18-mer/36-mer, 100 nM; pol ι, 1 μM, in 10-fold excess to DNA substrate to ensure single turnover conditions) with the metal-dCTP mixtures (2 mM MgCl$_2$ or 0.15 mM MnCl$_2$; dCTP, in varying concentrations), and then quenched with 0.15 M EDTA at time intervals from 0.15 to 30–120 s (or from 2 to 240–480 s for the R96G variant). MgCl$_2$ was supplemented by as much as the increase of dCTP to counterbalance the Mg^{2+}-chelating effect of dCTP for the reactions at high levels of dCTP. Reaction products were mixed with formamide-dye solution (20 mM EDTA, 95% formamide (v/v), 0.5% bromphenol blue (w/v), and 0.05% xylene cyanol (w/v)) and separated using an 8 M urea-containing denaturing gel with 16% polyacrylamide (w/v), and then quantified by a Bio-Rad Personal Molecular Imager instrument and the Quantity One software. Pre-steady-state data obtained under the single turnover condition were fit to the single-exponential equation $y = A(1 - \exp(-k_{obs}t))$, where y = concentration of product, A = reaction amplitude, k_{obs} = observed rate of nucleotide incorporation, and t = time (50, 51), using nonlinear regression analysis in GraphPad Prism software.

Determination of k_{pol} and $K_{d,dCTP}$—The pre-steady-state kinetic parameters k_{pol} and $K_{d,dCTP}$ were estimated by analyzing the dCTP dependence on the observed pre-steady-state rates of dCTP insertion under single turnover conditions. A graph of the observed rate (k_{obs}) versus dCTP concentration was fit to the hyperbolic equation $k_{obs} = [k_{pol}[dNTP]/([dNTP] + K_d)]$, where k_{pol} is the maximal rate of nucleotide incorporation and $K_{d,dCTP}$ is the equilibrium dissociation constant for dCTP (50, 51).

Crystallization of pol ι·dG-DNA·dCMPNPP Ternary Complexes in the presence of Mg^{2+} or Mn^{2+}—Crystals were obtained under the conditions previously reported (34, 36) with slight modifications described below. The purified pol ι enzymes (0.22 mM) were incubated with annealed self-complementary 18-mer DNA (5′-TCT GGG GTC CTA GGA CCC-3′, 0.26 mM) and 20 mM dCMPNPP (or 4 mM dCMPNPP for MnCl$_2$)

in the presence of 10 mM MgCl$_2$ (or 2 mM MnCl$_2$) on ice. The ternary complexes were crystallized in 0.1 M MES (pH 6.5), 0.2–0.4 M (NH$_4$)$_2$SO$_4$, and 10–22% polyethylene glycol 5000 (w/v) using the hanging-drop vapor diffusion method at 4 °C. Crystals were typically observed in 1–3 days. Crystals started to form with reservoir solutions containing 13–15, 18, and 18–20% polyethylene glycol monomethyl ether 5000 (w/v), respectively, for pol ι(26–445), pol ι(1–445), and R96G pol ι(1–445) ternary complexes. Crystals were mounted in nylon loops and cryoprotected in a reservoir solution containing 25% glycerol (v/v), and then flash-frozen in liquid nitrogen.

Structure Determination and Refinement—X-ray diffraction data were collected on the 21-ID-F (Life Sciences Collaborative Access Team (LS-CAT)) beam line at the Advanced Photon Source (Argonne National Laboratory, Argonne, IL). Collected data were indexed, integrated, and scaled using HKL2000 (52). All crystal types belonged to space group P6$_5$22. Structures were determined by molecular replacement phasing using the program Phaser MR (53) and the pol ι structure (PDB ID 2ALZ) as a search model. Structure refinements and model building were performed using PHENIX (54) and COOT (55). Metal coordination geometry was analyzed with UCSF Chimera (56). Structural illustrations were prepared with PyMOL (Schrödinger, LLC).

References

1. Helleday, T., Eshtad, S., and Nik-Zainal, S. (2014) Mechanisms underlying mutational signatures in human cancers. *Nat. Rev. Genet.* **15,** 585–598
2. Loeb, L. A., and Monnat, R. J., Jr. (2008) DNA polymerases and human disease. *Nat. Rev. Genet.* **9,** 594–604
3. Lange, S. S., Takata, K., and Wood, R. D. (2011) DNA polymerases and cancer. *Nat. Rev. Cancer* **11,** 96–110
4. Ling, H., Boudsocq, F., Woodgate, R., and Yang, W. (2001) Crystal structure of a Y-family DNA polymerase in action: a mechanism for error-prone and lesion-bypass replication. *Cell* **107,** 91–102
5. Choi, J.-Y., Eoff, R. E., and Guengerich, F. P. (2011) Bypass DNA polymerases. in *Chemical Carcinogenesis* (Penning, T. M., ed), pp. 345–373, Humana Press, New York, NY
6. Zhang, Y., Wu, X., Guo, D., Rechkoblit, O., Geacintov, N. E., and Wang, Z. (2002) Two-step error-prone bypass of the (+)- and (−)-trans-anti-BPDE-N^2-dG adducts by human DNA polymerases η and κ. *Mutat. Res.* **510,** 23–35
7. Zhang, Y., Wu, X., Rechkoblit, O., Geacintov, N. E., Taylor, J. S., and Wang, Z. (2002) Response of human REV1 to different DNA damage: preferential dCMP insertion opposite the lesion. *Nucleic Acids Res.* **30,** 1630–1638
8. Frank, E. G., Sayer, J. M., Kroth, H., Ohashi, E., Ohmori, H., Jerina, D. M., and Woodgate, R. (2002) Translesion replication of benzo[*a*]pyrene and benzo[*c*]phenanthrene diol epoxide adducts of deoxyadenosine and deoxyguanosine by human DNA polymerase ι. *Nucleic Acids Res.* **30,** 5284–5292
9. Avkin, S., Goldsmith, M., Velasco-Miguel, S., Geacintov, N., Friedberg, E. C., and Livneh, Z. (2004) Quantitative analysis of translesion DNA synthesis across a benzo[*a*]pyrene-guanine adduct in mammalian cells: the role of DNA polymerase κ. *J. Biol. Chem.* **279,** 53298–53305

10. Klarer, A. C., Stallons, L. J., Burke, T. J., Skaggs, R. L., and McGregor, W. G. (2012) DNA polymerase η participates in the mutagenic bypass of adducts induced by benzo[*a*]pyrene diol epoxide in mammalian cells. *PLoS ONE* **7,** e39596

11. Choi, J.-Y., Angel, K. C., and Guengerich, F. P. (2006) Translesion synthesis across bulky N^2-alkyl guanine DNA adducts by human DNA polymerase κ. *J. Biol. Chem.* **281,** 21062–21072

12. Choi, J.-Y., and Guengerich, F. P. (2005) Adduct size limits efficient and error-free bypass across bulky N^2-guanine DNA lesions by human DNA polymerase η. *J. Mol. Biol.* **352,** 72–90

13. Choi, J.-Y., and Guengerich, F. P. (2006) Kinetic evidence for inefficient and error-prone bypass across bulky N^2-guanine DNA adducts by human DNA polymerase ι. *J. Biol. Chem.* **281,** 12315–12324

14. Choi, J.-Y., and Guengerich, F. P. (2008) Kinetic analysis of translesion synthesis opposite bulky N^2- and O^6-alkylguanine DNA adducts by human DNA polymerase REV1. *J. Biol. Chem.* **283,** 23645–23655

15. Masutani, C., Kusumoto, R., Yamada, A., Dohmae, N., Yokoi, M., Yuasa, M., Araki, M., Iwai, S., Takio, K., and Hanaoka, F. (1999) The *XPV* (xeroderma pigmentosum variant) gene encodes human DNA polymerase η. *Nature* **399,** 700–704

16. Yoon, J. H., Prakash, L., and Prakash, S. (2009) Highly error-free role of DNA polymerase η in the replicative bypass of UV-induced pyrimidine dimers in mouse and human cells. *Proc. Natl. Acad. Sci. U.S.A.* **106,** 18219–18224

17. Kim, J., Song, I., Jo, A., Shin, J.-H., Cho, H., Eoff, R. L., Guengerich, F. P., and Choi, J.-Y.(2014) Biochemical analysis of six genetic variants of error-prone human DNA polymerase ι involved in translesion DNA synthesis. *Chem. Res. Toxicol.* **27,** 1837–1852

18. Song, I., Kim, E.-J., Kim, I.-H., Park, E.-M., Lee, K. E., Shin, J.-H., Guengerich, F. P., and Choi, J.-Y.(2014) Biochemical characterization of eight genetic variants of human DNA polymerase κ involved in error-free bypass across bulky N^2-guanyl DNA adducts. *Chem. Res. Toxicol.* **27,** 919–930

19. Yeom, M., Kim, I. H., Kim, J. K., Kang, K., Eoff, R. L., Guengerich, F. P., and Choi, J.-Y. (2016) Effects of twelve germline missense variations on DNA lesion and G-quadruplex bypass activities of human DNA polymerase REV1. *Chem. Res. Toxicol.* **29,** 367–379

20. Nair, D. T., Johnson, R. E., Prakash, S., Prakash, L., and Aggarwal, A. K. (2004) Replication by human DNA polymerase ι occurs by Hoogsteen base-pairing. *Nature* **430,** 377–380

21. Choi, J. Y., Lim, S., Eoff, R. L., and Guengerich, F. P. (2009) Kinetic analysis of base-pairing preference for nucleotide incorporation opposite template pyrimidines by human DNA polymerase ι. *J. Mol. Biol.* **389,** 264–274

22. Kirouac, K. N., and Ling, H. (2009) Structural basis of error-prone replication and stalling at a thymine base by human DNA polymerase ι. *EMBO J.* **28,** 1644–1654

23. Vaisman, A., Frank, E. G., Iwai, S., Ohashi, E., Ohmori, H., Hanaoka, F., and Woodgate, R. (2003) Sequence context-dependent replication of DNA templates containing UV-induced lesions by human DNA polymerase ι. *DNA Repair (Amst.)* **2,** 991–1006

24. Choi, J.-Y., Lim, S., Kim, E. J., Jo, A., and Guengerich, F. P. (2010) Translesion synthesis across abasic lesions by human B-family and Y-family DNA polymerases α, δ, η, ι, κ, and REV1. *J. Mol. Biol.* **404,** 34–44

25. Choi, J.-Y., Chowdhury, G., Zang, H., Angel, K. C., Vu, C. C., Peterson, L. A., and Guengerich, F. P. (2006) Translesion synthesis across O^6-alkylguanine DNA adducts by recombinant human DNA polymerases. *J. Biol. Chem.* **281,** 38244–38256

26. Dumstorf, C. A., Clark, A. B., Lin, Q., Kissling, G. E., Yuan, T., Kucherlapati, R., McGregor, W. G., and Kunkel, T. A. (2006) Participation of mouse DNA polymerase ι in strand-biased mutagenic bypass of UV photoproducts and suppression of skin cancer. *Proc. Natl. Acad. Sci. U.S.A.* **103,** 18083–18088

27. Iguchi, M., Osanai, M., Hayashi, Y., Koentgen, F., and Lee, G. H. (2014) The error-prone DNA polymerase ι provides quantitative resistance to lung tumorigenesis and mutagenesis in mice. *Oncogene* **33,** 3612–3617

28. Ohkumo, T., Kondo, Y., Yokoi, M., Tsukamoto, T., Yamada, A., Sugimoto, T., Kanao, R., Higashi, Y., Kondoh, H., Tatematsu, M., Masutani, C., and Hanaoka, F. (2006) UV-B radiation induces epithelial tumors in mice lacking DNA polymerase η and mesenchymal tumors in mice deficient for DNA polymerase ι. *Mol. Cell Biol.* **26,** 7696–7706

29. Albertella, M. R., Lau, A., and O'Connor, M. J. (2005) The overexpression of specialized DNA polymerases in cancer. *DNA Repair (Amst.)* **4,** 583–593

30. Yang, J., Chen, Z., Liu, Y., Hickey, R. J., and Malkas, L. H. (2004) Altered DNA polymerase ι expression in breast cancer cells leads to a reduction in DNA replication fidelity and a higher rate of mutagenesis. *Cancer Res.* **64,** 5597–5607

31. Yuan, F., Xu, Z., Yang, M., Wei, Q., Zhang, Y., Yu, J., Zhi, Y., Liu, Y., Chen, Z., and Yang, J. (2013) Overexpressed DNA polymerase ι regulated by JNK/c-Jun contributes to hypermutagenesis in bladder cancer. *PLoS ONE* **8,** e69317

32. Zhou, J., Zhang, S., Xie, L., Liu, P., Xie, F., Wu, J., Cao, J., and Ding, W. Q. (2012) Overexpression of DNA polymerase ι (pol ι) in esophageal squamous cell carcinoma. *Cancer Sci.* **103,** 1574–1579

33. Frank, E. G., and Woodgate, R. (2007) Increased catalytic activity and altered fidelity of human DNA polymerase ι in the presence of manganese. *J. Biol. Chem.* **282,** 24689–24696

34. Pence, M. G., Blans, P., Zink, C. N., Hollis, T., Fishbein, J. C., and Perrino, F. W. (2009) Lesion bypass of N^2-ethylguanine by human DNA polymerase ι. *J. Biol. Chem.* **284,** 1732–1740

35. Batra, V. K., Beard, W. A., Shock, D. D., Krahn, J. M., Pedersen, L. C., and Wilson, S. H. (2006) Magnesium-induced assembly of a complete DNA polymerase catalytic complex. *Structure* **14,** 757–766

36. Nair, D. T., Johnson, R. E., Prakash, L., Prakash, S., and Aggarwal, A. K. (2005) Human DNA polymerase ι incorporates dCTP opposite template G via a G.C$^+$ Hoogsteen base pair. *Structure* **13,** 1569–1577

37. Yang, W., Lee, J. Y., and Nowotny, M. (2006) Making and breaking nucleic acids: two-Mg^{2+}-ion catalysis and substrate specificity. *Mol. Cell* **22,** 5–13

38. Zhao, Y., Biertümpfel, C., Gregory, M. T., Hua, Y. J., Hanaoka, F., and Yang, W. (2012) Structural basis of human DNA polymerase η-mediated chemoresistance to cisplatin. *Proc. Natl. Acad. Sci. U.S.A.* **109,** 7269–7274

39. Koag, M. C., Lai, L., and Lee, S. (2014) Structural basis for the inefficient nucleotide incorporation opposite cisplatin-DNA lesion by human DNA polymerase β. *J. Biol. Chem.* **289,** 31341–31348

40. Nair, D. T., Johnson, R. E., Prakash, L., Prakash, S., and Aggarwal, A. K. (2006) An incoming nucleotide imposes an *anti* to *syn* conformational change on the templating purine in the human DNA polymerase-ι active site. *Structure* **14,** 749–755

41. Xia, S., Wang, M., Blaha, G., Konigsberg, W. H., and Wang, J. (2011) Structural insights into complete metal ion coordination from ternary complexes of B family RB69 DNA polymerase. *Biochemistry* **50,** 9114–9124

42. Batra, V. K., Beard, W. A., Shock, D. D., Pedersen, L. C., and Wilson, S. H. (2008) Structures of DNA polymerase β with active-site mismatches suggest a transient abasic site intermediate during misincorporation. *Mol. Cell* **30,** 315–324

43. Koag, M. C., Nam, K., and Lee, S. (2014) The spontaneous replication error and the mismatch discrimination mechanisms of human DNA polymerase β. *Nucleic Acids Res.* **42,** 11233–11245

44. Vashishtha, A. K., and Konigsberg, W. H. (2016) Effect of different divalent cations on the kinetics and fidelity of RB69 DNA polymerase. *Biochemistry* **55,** 2661–2670

45. Blanca, G., Shevelev, I., Ramadan, K., Villani, G., Spadari, S., Hübscher, U., and Maga, G. (2003) Human DNA polymerase λ diverged in evolution from DNA polymerase β toward specific Mn^{2+} dependence: a kinetic and thermodynamic study. *Biochemistry* **42,** 7467–7476

46. Vaisman, A., Ling, H., Woodgate, R., and Yang, W. (2005) Fidelity of Dpo4: effect of metal ions, nucleotide selection and pyrophosphorolysis. *EMBO J.* **24,** 2957–2967

47. García-Gómez, S., Reyes, A., Martínez-Jiménez, M. I., Chocrón, E. S., Mourón, S., Terrados, G., Powell, C., Salido, E., Méndez, J., Holt, I. J., and Blanco, L. (2013) PrimPol, an archaic primase/polymerase operating in human cells. *Mol. Cell* **52,** 541–553

48. Gao, Y., and Yang, W. (2016) Capture of a third Mg^{2+} is essential for catalyzing DNA synthesis. *Science* **352,** 1334–1337

49. Johnson, R. E., Trincao, J., Aggarwal, A. K., Prakash, S., and Prakash, L. (2003) Deoxynucleotide triphosphate binding mode conserved in Y family DNA polymerases. *Mol. Cell Biol.* **23,** 3008–3012

50. Johnson, K. A. (1995) Rapid quench kinetic analysis of polymerases, adenosinetriphosphatases, and enzyme intermediates. *Methods Enzymol.* **249,** 38–61

51. Joyce, C. M. (2010) Techniques used to study the DNA polymerase reaction pathway. *Biochim. Biophys. Acta* **1804,** 1032–1040

52. Otwinowski, Z., and Minor, W. (1997) Processing of x-ray diffraction data collected in oscillation mode. *Methods Enzymol.* **276,** 307–326

53. McCoy, A. J., Grosse-Kunstleve, R. W., Adams, P. D., Winn, M. D., Storoni, L. C., and Read, R. J. (2007) Phaser crystallographic software. *J. Appl. Crystallogr.* **40,** 658–674

54. Adams, P. D., Afonine, P. V., Bunkóczi, G., Chen, V. B., Davis, I. W., Echols, N., Headd, J. J., Hung, L. W., Kapral, G. J., Grosse-Kunstleve, R. W., McCoy, A. J., Moriarty, N. W., Oeffner, R., Read, R. J., Richardson, D. C., *et al.* (2010) PHENIX: a comprehensive Python-based system for macromolecular structure solution. *Acta Crystallogr. D Biol. Crystallogr.* **66,** 213–221

55. Emsley, P., Lohkamp, B., Scott, W. G., and Cowtan, K. (2010) Features and development of Coot. *Acta Crystallogr. D Biol. Crystallogr.* **66,** 486–501

56. Pettersen, E. F., Goddard, T. D., Huang, C. C., Couch, G. S., Greenblatt, D. M., Meng, E. C., and Ferrin, T. E. (2004) UCSF Chimera: a visualization system for exploratory research and analysis. *J. Comput. Chem.* **25,** 1605–1612